

Equilibrium grain boundary segregation and clustering of impurities in colloidal polycrystalline monolayers

François A. Lavergne,^{*} Samuel Diana, Dirk G. A. L. Aarts, and Roel P. A. Dullens

Department of Chemistry, Physical and Theoretical Chemistry Laboratory, University of Oxford, South Parks Road, Oxford, OX1 3QZ, United Kingdom.

E-mail: francois.lavergne@chem.ox.ac.uk

Abstract

We investigate the segregation of impurities to grain boundaries in colloidal polycrystalline monolayers using video-microscopy. A model colloidal alloy is prepared by embedding large spherical impurities in a polycrystalline monolayer of small host colloidal hard spheres, which stops grain growth at a finite grain size. The size ratio between the impurities and the host particles determines whether they behave as interstitial or substitutional impurities in the bulk crystal, akin to those in real alloys. We find that the partitioning of impurities between the grains and the grain boundaries is in very good agreement with the Langmuir-McLean adsorption model for equilibrium grain boundary segregation. This enables the direct measurement of the free energy of adsorption for the two types of impurities. Near saturation, we characterise the spatial distribution of the adsorbed impurities and find that it strongly depends on their interstitial or substitutional nature. This is because the relative importance of clustering and mixing due to non-additivity is determined by geometrical constraints imposed by the crystalline host lattice.

Introduction

The process of alloying, i.e. the incorporation of solute atoms of one or several other elements in

a metal, can dramatically change the properties of a material.¹ For example, solute atoms, or impurities, can interact with grain boundaries (GBs) via impurity drag^{2,3} or Zener pinning,³⁻⁵ which stops the grain growth process at a finite grain size.^{1,6,7} Controlling the grain size is key in tuning the mechanical properties of a material due to the Hall-Petch effect, which predicts that the strength of a material sensitively depends on the grain size.⁸⁻¹⁰

In a polycrystalline alloy, impurities tend to be adsorbed at GBs, as they offer more free volume than the grains, a phenomenon known as GB segregation.^{11,12} This is analogous to the adsorption of a gas onto a solid surface, with the impurity concentration in the bulk crystal being akin to the pressure of the gas.^{11,13,14} At equilibrium, in the ideal case where there are no interactions between adsorbed atoms, the surface coverage as a function of the pressure in the gas phase is given by the Langmuir adsorption model.^{15,16} The counterpart of this model for the case of GB segregation is the McLean model,¹¹ which considers impurities distributed on a lattice comprising of crystal sites and GB sites. The fractions of crystal and GB sites occupied by impurities are denoted by X_b and X_{gb} , respectively. At equilibrium, these two quantities are related to each other via the Langmuir-McLean isotherm,

$$\frac{X_{gb}}{X_{gb}^{sat}} = \frac{KX_b}{1 + KX_b}, \quad (1)$$

where X_{gb}^{sat} is the value of X_{gb} at saturation and $K = \exp(e_a/k_B T)$ the equilibrium constant, with e_a being the free-energy of adsorption. In the limit of small X_b , X_{gb} is expected to increase linearly with X_b as the denominator in Eq. (1) is close to unity. Good agreement of this model with experimental data was found for different alloys.^{17,18} Nevertheless, different behaviours can be observed depending on e.g. the solute-solvent interactions, the solute-solvent size ratio and the lattice structure.^{12,14}

Colloidal polycrystalline systems with embedded impurities have already been proven to be good model systems to directly visualise GB segregation using brightfield or confocal microscopy.^{19–22} The impurities are usually colloidal particles with a different size than that of the host particles. Such systems have been used to investigate grain size control^{20,23} and the dynamics of segregation during crystallisation in great detail.^{24–26} Monolayers of colloidal spheres with added impurities of a different size are also very interesting from a more fundamental point of view as they provide a simple realisation of a non-additive binary system.^{27,28} Such mixtures exhibit very rich phase behaviour caused by the clustering of the impurity particles due to depletion effects.^{27–30}

In this work, we study GB segregation in a polycrystalline monolayer of hard spheres with embedded impurities using video-microscopy. We use impurities of two different sizes and show that their size ratio with the host particles determines whether they behave as interstitial or substitutional impurities in the bulk crystal. We find that their segregation behaviour is in very good agreement with the Langmuir-McLean model of equilibrium adsorption and directly measure the free energy of adsorption in both cases. The spatial distribution of impurities close to saturation highlights different relative contributions of clustering and mixing due to non-additivity depending on the type of impurities. These differences are shown to originate from the geometrical constraints imposed by the lattice.

Methods

Preparation of “colloidal alloys”

Our experimental system consists of colloidal polycrystalline monolayers with added larger colloidal particles, termed impurities. The host particles forming the polycrystalline monolayer are melamine formaldehyde spheres (Microparticles GmbH) of diameter $\sigma_s = 2.7 \mu\text{m}$, dispersed in a 20/80 $v/v\%$ isopropanol/water mixture. The added impurities are melamine formaldehyde spheres of diameter $\sigma_i = 6.1 \mu\text{m}$ or $10.8 \mu\text{m}$. The particles are contained in a 200 μm thick quartz cell (Hellma Analytics) and due to their high mass density (1.51 g/cm^3), they sediment to the bottom wall of the cell within a few minutes to form a monolayer. In these conditions, it has been showed that these particles behave as hard spheres in a quasi two-dimensional system as the out-of-plane fluctuations are negligible.³¹

Impurity-doped polycrystalline monolayers are prepared with different concentrations of impurities. The sample cell is placed on a levelled microscope stage (Olympus CKX41) and the polycrystalline monolayer is left to coarsen until grain growth has stopped due to the presence of impurities. All the samples are prepared 24 hours before data acquisition to ensure this stationary regime has been reached. Images of the polycrystalline structures are recorded using a 20 \times objective and a CMOS camera (Ximea XiQ). As the area of the sample cell is much bigger than the area of interest, images containing $\sim 4 \times 10^4$ particles are taken at different locations within the monolayer to improve statistics for a given concentration of impurities. This is necessary as the fluctuations in the number of impurities per frame can be significant, especially when their concentration is small.

Composition variables

The confinement of the host and impurity particles to a monolayer leads to non-additivity as the effective impurity size in the plane of the smaller host particles, σ'_i , can be significantly

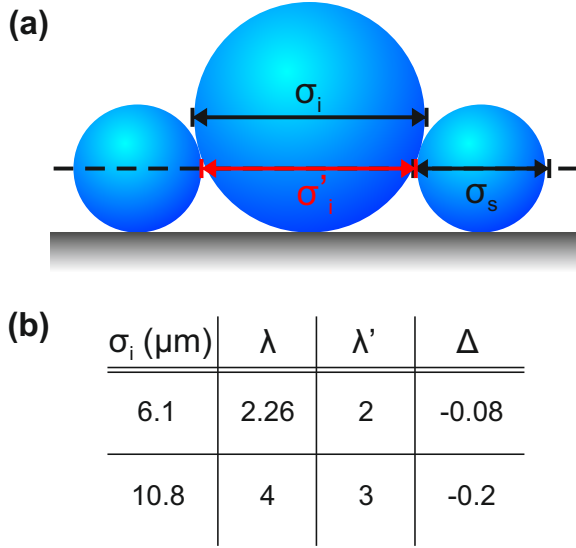


Figure 1: Schematic view of close-packed hard spheres of two different sizes arranged in a monolayer. The diameters of the small and large particles are denoted σ_s and σ_i respectively. The effective diameter in the plane of the small particles (dashed line) is denoted σ'_i . (b) Characteristics of the two types of impurity particles: diameter σ_i , real and in-plane size ratios λ and λ' , together with the non-additivity parameter Δ (Eq. (4)).

different from the actual impurity size, σ_i (see Fig. 1(a)). Using elementary geometry, the effective in-plane impurity size, σ'_i in Fig. 1(a), is found as

$$\sigma'_i = \sigma_s \left(2\sqrt{\frac{\sigma_i}{\sigma_s}} - 1 \right). \quad (2)$$

The non-additivity is quantified by the non-additivity parameter, Δ , defined by^{29,30}

$$\frac{\sigma_s + \sigma'_i}{2} = \frac{\sigma_s + \sigma_i}{2}(1 + \Delta). \quad (3)$$

Defining the actual and in-plane size ratios between the impurities and the host particles as $\lambda = \sigma_i/\sigma_s$ and $\lambda' = \sigma'_i/\sigma_s$, the non-additivity parameter can be written as

$$\Delta = \frac{\lambda' - \lambda}{\lambda + 1}. \quad (4)$$

The characteristic geometrical quantities of the two types of impurities are given in Fig. 1(b),

showing that Δ is negative and that the in-plane size ratios are integers in both cases.

To characterise the partitioning of impurities between the bulk and the grain boundaries, we define the composition of the bulk crystal, Q_b , and that of the GBs, Q_{gb} , by

$$Q_b = \frac{\lambda'^2 N_i^b}{N_s^b + \lambda'^2 N_i^b}, \quad (5a)$$

$$Q_{gb} = \frac{\lambda'^2 N_i^{gb}}{N_s^{gb} + \lambda'^2 N_i^{gb}}. \quad (5b)$$

Here, N_s^b (N_s^{gb}) is the number of host particles in the bulk (GBs,) and N_i^b (N_i^{gb}) the number of impurities in the bulk (GBs). Note that both Q_b and Q_{gb} vary between 0 and 1, corresponding to the cases where no or only impurities are present in the bulk crystal and the GBs, respectively.

Detection of adsorbed impurities

Standard image analysis routines are used to obtain the coordinates of the particles in each frame,³² and the impurity particles are easily discriminated from the host particles based on their size and brightness, see Fig. 2(a).

To quantify the local crystalline order of a particle j , we use the bond-orientational order parameter defined by³³

$$\psi_6(\vec{r}_j) = \frac{1}{N_j} \sum_{k=1}^{N_j} e^{i6\Delta\theta_{jk}}, \quad (6)$$

where $\Delta\theta_{jk}$ is the angle between the x -direction and the bond vector connecting the particle j to one of its N_j nearest neighbours k , defined using a Delaunay triangulation (Fig. 2(a), inset). The ψ_6 -field is subsequently coarse-grained by replacing its value at \vec{r}_j by the average over the two shells of nearest neighbours of the particle j (Fig. 2(a), inset), which helps defining the grains better by removing small fluctuations of ψ_6 . The local orientation is then given by $\theta_6 = \arg(\psi_6)/6$, and varies from 0 to 60° due to the hexagonal symmetry of the 2D crystal. An example of the local orientation map is shown in Fig. 2(b) for $\lambda' = 3$, where an impurity in a

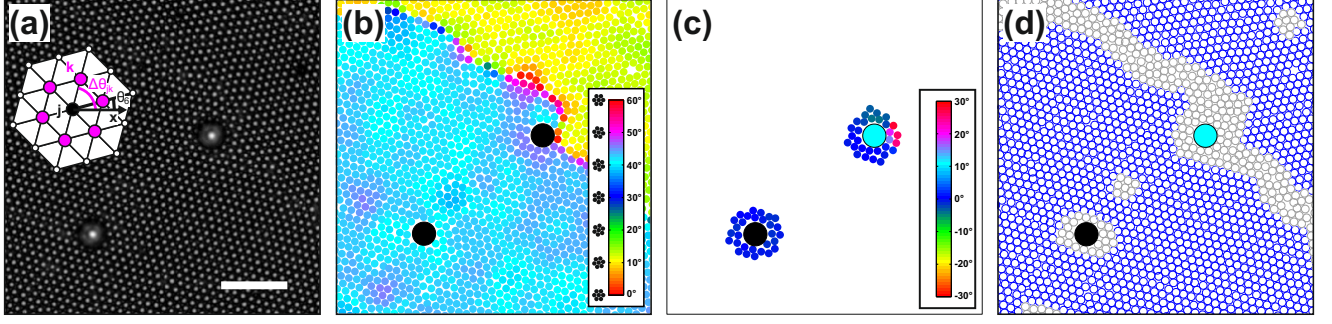


Figure 2: (a) Image of a small area of a colloidal polycrystalline monolayer containing impurities of size ratio $\lambda' = 3$. The inset shows the parameters used to define ψ_6 and θ_6 (see text). Scale bar, 30 μm . (b) Output of the particle detection where impurities are black disks and host particles are coloured according to their orientation θ_6 , indicated by the colourbar. (c) The impurities with their two shells of nearest neighbours, coloured according to the value of their orientation relative to the mean, θ_6^0 (see Eq. (7)), as indicated by the colourbar. The impurity successfully detected as belonging to the grain boundary is coloured in cyan. (d) The crystal and GB host particles coloured in blue and grey, respectively, with the two discriminated impurities.

grain and one in a GB can be seen.

To determine whether impurities are located in grains or adsorbed at GBs, a procedure is developed based on the local orientation around impurities, as this is uniform if they lie inside a grain and strongly varies if they are located at a GB. Firstly, for every impurity, the two shells of nearest neighbours are selected, a set denoted S_2 (see Fig. 2(c)). Next, for each particle $j \in S_2$, the orientation relative to the mean is defined as

$$\theta_6^0(\vec{r}_j) = \frac{1}{6} \arg \left(\frac{\psi_6(\vec{r}_j)}{\langle \psi_6(\vec{r}_k) \rangle_{k \in S_2}} \right), \quad (7)$$

where $\langle . \rangle$ denotes the average over S_2 and the argument is taken in the interval $(-\pi/6; \pi/6]$. By definition, θ_6^0 is always distributed around 0, which avoids having the discontinuity between 0 and $\pi/3$ present in the θ_6 -field due to the 6-fold symmetry. The neighbours of impurity particles adsorbed at GBs typically have large values of θ_6^0 , while neighbours of bulk impurities have θ_6^0 values close to 0, as can be seen from Fig. 2(c). Finally, an impurity is considered as adsorbed at a GB if at least 3 particles in its neighbourhood S_2 have $|\theta_6^0| > 3^\circ$. The value of this cut-off was chosen by trial and error on representative snapshots, and Fig. 2(d) shows that the impurity adsorbed in the GB is successfully identified by the algorithm. When performed

on a whole snapshot, this analysis enables the direct measurement of the number of impurities in the bulk, N_i^b , and in the GBs, N_i^{gb} .

To discriminate between the host particles belonging to crystalline grains and the GBs, the following criterion is applied: a host particle j is considered to be in a GB if $|\psi_6(\vec{r}_j)| < 0.7$, otherwise, it belongs to a crystalline grain.³⁴ Figure 2(d) shows the crystalline host particles in blue and the GB ones in grey. The latter correspond well to the GBs, but also include distorted layers around bulk impurities. The numbers of host particles in the bulk crystal and in the GBs, N_s^b and N_s^{gb} , together with N_i^b and N_i^{gb} , are used to determine the composition of the bulk and the GBs, Q_b and Q_{gb} , according to Eq. (5a) and Eq. (5b).

Results and discussion

Characterisation of impurities

We first characterise the behaviour of the impurities in the pure crystal by considering microscopy images of isolated impurities embedded in the bulk crystal for both size ratios, see Fig. 3(a). The corresponding computer reconstructions of these two snapshots are shown in Fig. 3(b), where each particle is represented by a disk with the relevant hard core diameter. For

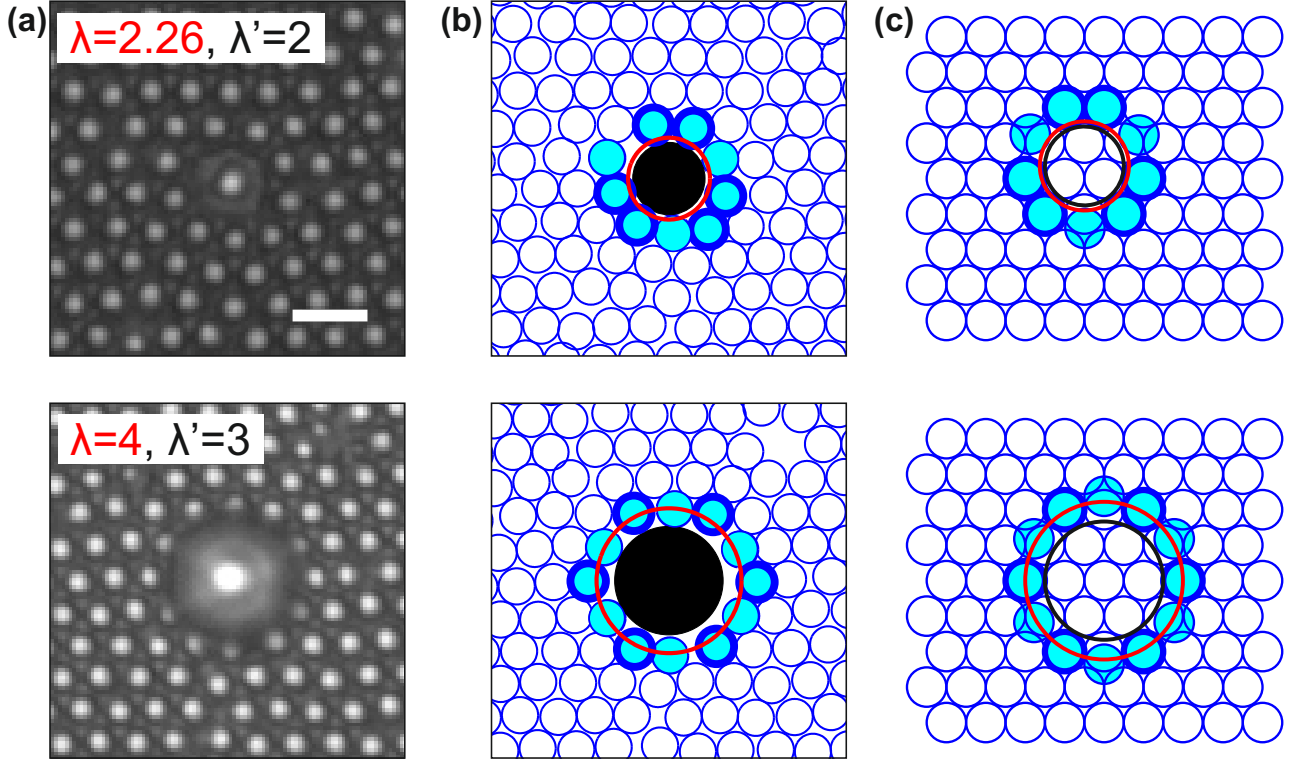


Figure 3: (a) Microscopy images of isolated impurities of each size embedded in the crystal. Scale bar, $5\text{ }\mu\text{m}$. (b) Corresponding reconstructions of the images where each particle is represented by a disk with the relevant hard sphere diameter. Host particles are in blue with diameter σ_s , and the impurities are represented by a black disk of diameter σ'_i and a red circle of diameter σ_i . The first shell of nearest neighbours is coloured in cyan, and the thick circles highlight particles in coincidence with the crystal. (c) Equivalent geometric constructions on an ideal lattice with the same colour code, showing that the center of mass of an impurity with $\lambda' = 2$ occupies an interstitial site, while it occupies a crystal site for an impurity with $\lambda' = 3$.

the host particles (blue) this is σ_s , while for the impurity particles two disks of diameters σ_i (the actual size, in red) and σ'_i (the in-plane size defined in Eq. (2), in black) are used. The nearest neighbours (cyan) are arranged in a ring around the impurities, which is partly distorted compared to the bulk crystal structure, though the latter is recovered at longer distances.^{19,35} Note that the overhang results in the host particles next to the impurities ($\lambda' = 3$) appearing slightly dimmer and smaller. We verified using inverted confocal microscopy in reflection mode³⁶ that these particles are located in the same plane as the other host particles (see Supporting Information, Fig. S1).

Interestingly, none of the impurities introduce any dislocations in the lattice as Burgers circuits drawn around them close up in a perfect

lattice.³³ This is consistent with these impurities either being located at a lattice site or an interstitial site. We discriminated between these two cases by overlaying a disk of diameter σ'_i on a perfect hexagonal lattice and looking for the configuration that maximises the number of nearest neighbours that coincide with bulk lattice sites (thick circles in Fig. 3(b) and (c)). The best matching situations are shown in Fig. 3(c), where the impurity is located at an interstitial site in the case of $\lambda' = 2$, and at a lattice site in the case of $\lambda' = 3$. In fact, these plots show that impurities with $\lambda' = 2$ behave as interstitial impurities, while impurities with $\lambda' = 3$ behave as substitutional impurities. We use this terminology, which is based on their behaviour within the crystalline grains, to distinguish the impurities throughout the remainder of the pa-

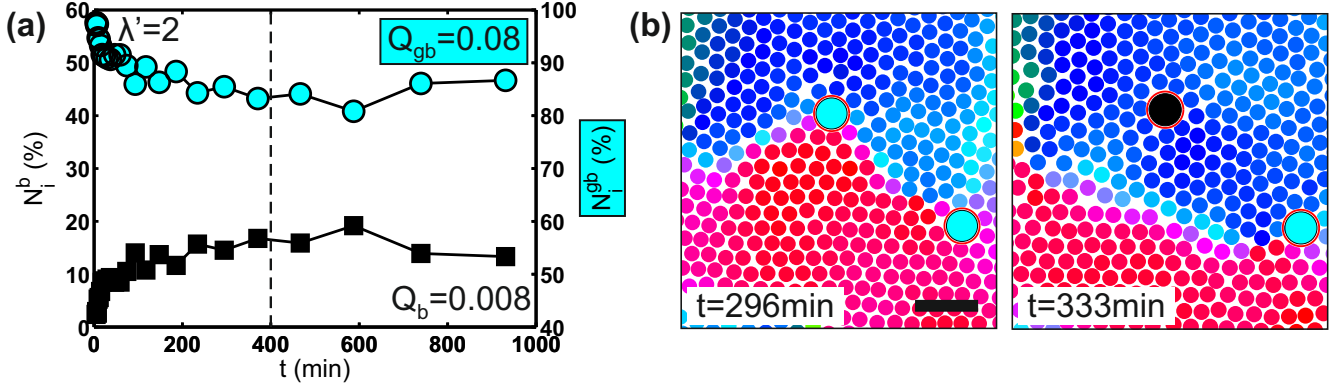


Figure 4: (a) Time evolution of the number of impurities within the grains, N_i^b , and that of impurities adsorbed at GBs, N_i^{gb} , expressed as a percentage of the total number of impurities, $N_i^b + N_i^{gb}$. From $t \simeq 400$ min after sample preparation (dashed line), a stationary regime is reached (see Movie S1). The compositions of the grains and the GBs (see Eq. (5a) and Eq. (5b)) are given 24 hours after sample preparation, when the stationary regime is well established. (b) De-pinning of an impurity during GB migration (see Movie S2). The impurities are shown in black if in a grain and in cyan if adsorbed at a GB. Scale bar, 10 μm .

per. Note that in metallurgy, however, interstitial impurities are usually smaller than the atoms constituting the crystal, in contrast to the present case.

Dynamics of segregation during grain growth

In order to confirm that a stationary regime has been reached 24 hours after sample preparation, we monitor the dynamics of impurity partitioning during grain growth. Figure 4(a) shows the time evolution of N_i^b and N_i^{gb} until about 16 hours after sample preparation, in the case of $\lambda' = 2$. One can clearly see that both curves flatten after $t \simeq 400$ min, indicating that a stationary regime has been reached with constant impurity compositions in the bulk grains and GBs (see Movie S1). Thus by measuring the compositions of the grains and the GBs, Q_b and Q_{gb} , 24 hours after sample preparation, we ensure that these values corresponds to those in the stationary regime.

Figure 4(a) also gives important insight into the dynamics of the segregation process. Indeed, it clearly shows that N_i^b increases in time while N_i^{gb} decreases, indicating that, effectively, a fraction of impurities initially in GBs ends up in the bulk grains. This happens by de-pinning

of impurities initially located in GBs during GB migration as shown in Fig. 4(b) and Movie S2. The stationary regime is reached when the average curvature of GBs is so low that GB migration cannot overcome the pinning force,¹ which causes grain growth to stop (see Movie S1).

Equilibrium segregation and adsorption isotherms

Figure 5 shows partial views of polycrystalline structures in the stationary regime for three values of the bulk composition, $Q_b = 10^{-3}$, 10^{-2} and 10^{-1} . The impurities are coloured in black if embedded in a grain and in cyan if adsorbed at a GB. Most impurities clearly populate the GBs, which indicates that GB segregation is occurring in the system. The tendency of impurities to segregate at GBs can be explained by the fact that the strain energy is much lower in the case of an impurity located at a GB than in the case of an impurity embedded in the bulk crystal.¹² The grain size is observed to decrease with increasing Q_b , confirming that the addition of impurities is a way to control the grain size.^{23,37} Notably, at $Q_b = 10^{-3}$ and for both size ratios, only a few impurity particles are adsorbed at GBs, which is already sufficient to stop grain growth. Next, for $Q_b = 10^{-2}$, signif-

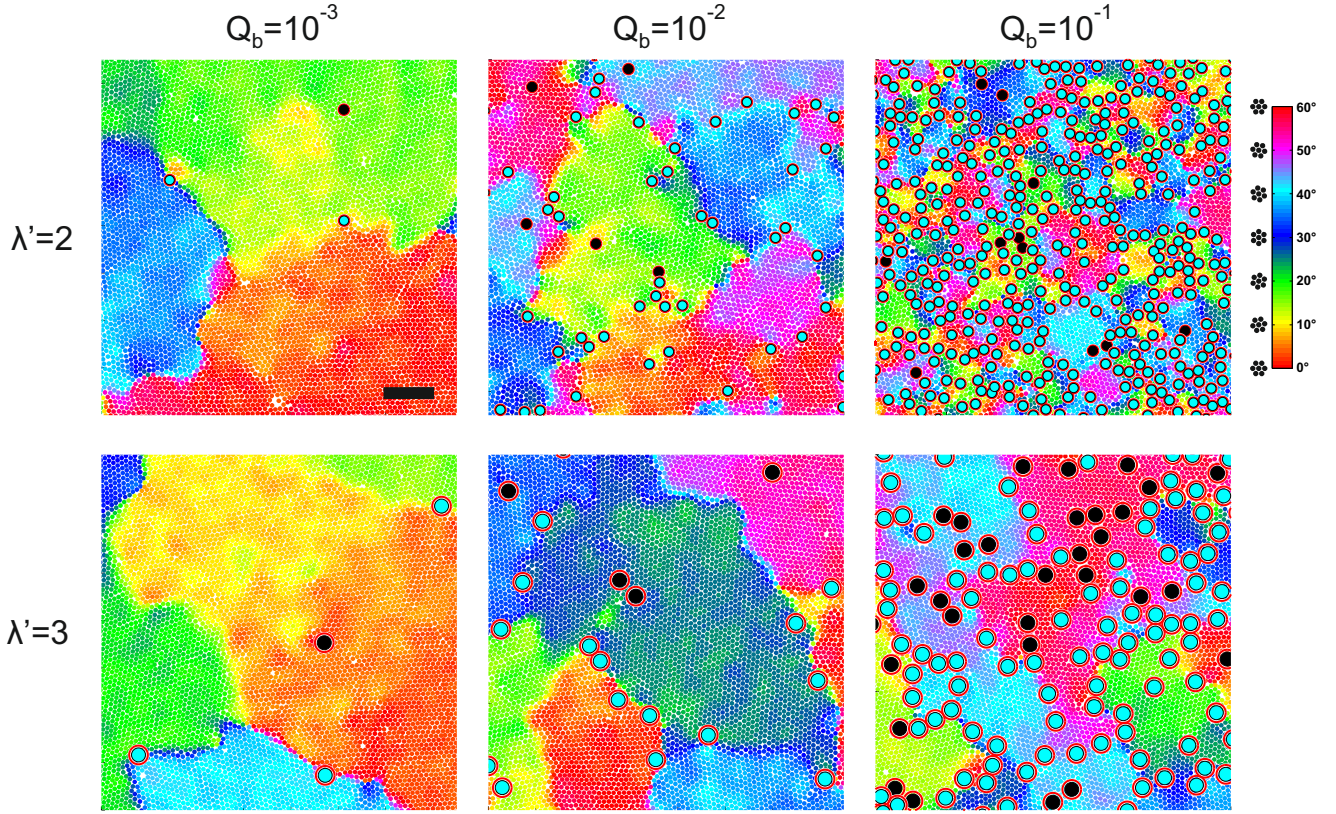


Figure 5: Partial views of the polycrystalline monolayer for the two types of impurities, characterised by their in-plane size ratio λ' , at three different bulk impurity compositions Q_b . The host particles are coloured according to their local orientation (see colourbar) while the impurities are shown in black if in a grain and in cyan if adsorbed at a GB. The red circles correspond to the actual dimensions of the impurities. Scale bar, 30 μm .

icantly more impurities are located at the GBs compared to the number of impurities in the grains, clearly indicating further GB segregation, while the sample remains polycrystalline. Finally, in the case of $Q_b = 10^{-1}$, the GBs are loaded with many impurities and the polycrystalline nature is preserved. Note, however, that some areas of the sample look quite disordered, especially for $Q_b = 10^{-1}$ and $\lambda' = 2$. This is consistent with a recent study on colloidal microgels, which showed that high impurity concentrations can lead to vitrification.³⁸

Next, we quantify the GB segregation by determining the adsorption isotherms, i.e. plotting Q_{gb} as a function of Q_b , as shown in Fig. 6(a) and (b) for interstitial ($\lambda' = 2$) and substitutional ($\lambda' = 3$) impurities, respectively. In both cases, the data covers the dilute regime, where Q_{gb} increases linearly up

to $Q_b \sim 10^{-2}$. A more concentrated regime can be observed, where the curves flatten approaching saturation around $Q_b \sim 10^{-1}$. The solid lines correspond to fits to the Langmuir-McLean isotherm, Eq. (1), for each size ratio, but now rewritten in terms of composition variables:

$$Q_{gb} = Q_{gb}^{sat} \frac{KQ_b}{1 + KQ_b}. \quad (8)$$

Here, the GB composition at saturation, Q_{gb}^{sat} , and the equilibrium constant, K , are the fitting parameters. As can be seen from Fig. 6(a) and (b), the Langmuir-McLean model describes the experimental data very well, indicating that equilibrium between the impurity content of the GBs and the grains has been reached.

The saturation levels for the two size ratios are very similar as the fits give $Q_{gb}^{sat} = 0.40 \pm 0.07$ for $\lambda' = 2$ and 0.37 ± 0.07

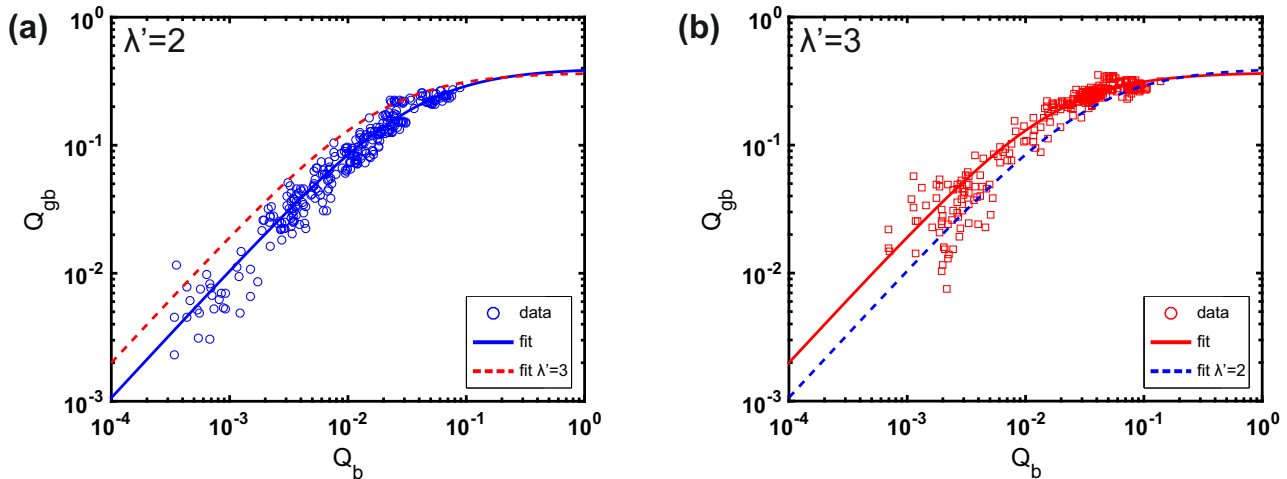


Figure 6: (a) Variation of the GB composition Q_{gb} as a function of the bulk composition Q_b for interstitial impurities ($\lambda' = 2$). (b) Same data for substitutional impurities ($\lambda' = 3$). The solid lines are fits to the Langmuir-McLean theory and the dashed lines correspond to the fitted curve for the other size ratio on each graph to allow for direct comparison. The fits give equilibrium constants of $K = 26.76 \pm 3.17$ and 54.33 ± 5.93 for $\lambda' = 2$ and 3, respectively.

for $\lambda' = 3$. Interestingly, these values are significantly below unity, indicating that saturation does not correspond to a GB fully covered by impurities. In fact, the majority of the distorted sites constituting the GBs are still vacant as Q_{gb}^{sat} is well below 0.5. Studies of GB segregation in metals also report partial coverage at saturation in most cases.^{12–14}

Importantly, we can directly determine the free energy of adsorption from the isotherm via $e_a/k_B T = \ln(K)$. The obtained adsorption free energies are $e_a/k_B T = 3.29 \pm 0.12$ for $\lambda' = 2$ and 4.00 ± 0.11 for $\lambda' = 3$. Thus the large impurities have a larger adsorption free energy than the small impurities, leading to a higher coverage of the GBs at equal Q_b (see Fig. 6). Interestingly, the adsorption free energy has an entropic origin as there are only hard core interactions in this system. The value of the adsorption free energy is only a few $k_B T$ in both cases, indicating that adsorption at GBs is reversible. This corroborates the idea that the observed GB segregation corresponds to equilibrium segregation, as already suggested by the agreement with the Langmuir-McLean model.

Overall, the interstitial or substitutional character of the impurities has little impact on the values of Q_{gb}^{sat} and e_a , which are in fact fairly comparable for both cases. Indeed, in our hard

sphere system, the main contribution to the strain energy is the size mismatch between the impurities and the host particles, λ' . As the values of λ' for both types of impurities are fairly similar, the strain energies – and hence the values of Q_{gb}^{sat} and e_a – are not expected to be very different. However, we show in the remainder of the paper that the interstitial or substitutional character induces structural differences concerning the impurities adsorbed at GBs.

Distribution of impurities at grain boundaries

Pair correlation function

Next, we analyse the spatial distribution of impurities in the GBs close to saturation for both size ratios, i.e. for interstitial ($\lambda' = 2$) and substitutional impurities ($\lambda' = 3$). To this end, the pair correlation function, $g(r)$, of the impurities located at GBs *only* is computed according to

$$g(r) = \frac{\pi \sigma_i'^2}{4 N_i^{gb} \phi_i^{gb}} \left\langle \sum_{j=1}^{N_i^{gb}} \sum_{k \neq j} \delta(\vec{r} - \vec{r}_j + \vec{r}_k) \right\rangle, \quad (9)$$

for samples having Q_{gb} close to the saturation level. Here, ϕ_i^{gb} denotes the area fraction of adsorbed impurities defined by

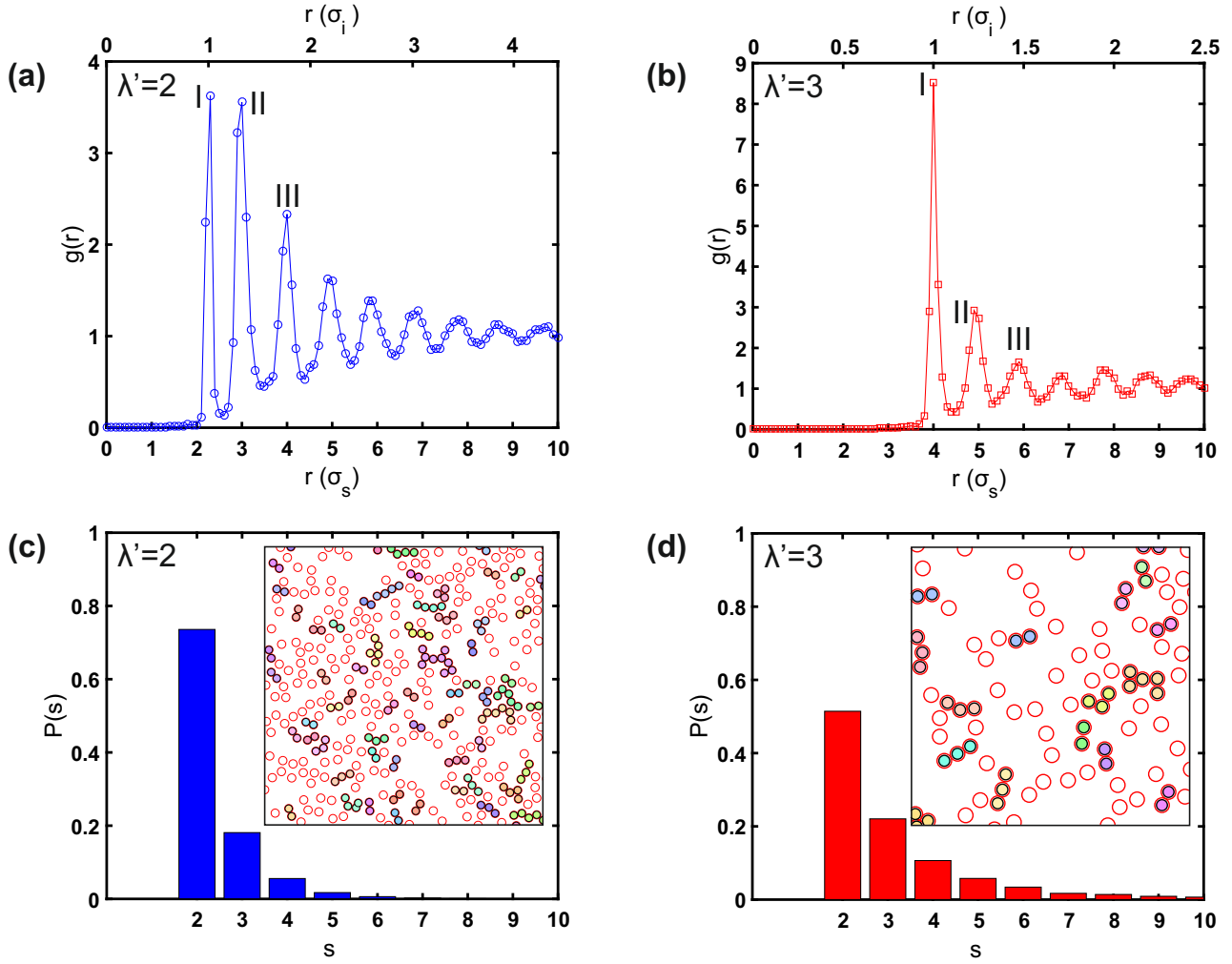


Figure 7: (a) Average pair correlation function of interstitial impurities ($\lambda' = 2$) adsorbed at GBs for samples of composition $Q_{gb} = 0.24 \pm 0.02$. The first three peaks (I, II and III) are described in the text. (b) The same quantity for the substitutional impurities ($\lambda' = 3$) with $Q_{gb} = 0.30 \pm 0.03$. (c) Size distribution of the clusters of two or more GB interstitial impurities ($\lambda' = 2$), dominated by the presence of dimers. The data is the same as in (a). The inset shows a representative partial view of the clusters (colours) together with isolated impurities (circles), which corresponds to Fig. 5 for $Q_b = 10^{-1}$ and $\lambda' = 2$. (d) Same as in (c) for substitutional impurities ($\lambda' = 3$). The decay of the distribution is much smoother indicating the presence of larger clusters at the expense of dimers.

$\phi_i^{gb} = N_i^{gb} \pi \sigma_i'^2 / (4A)$, where A is the area of the field of view. Figure 7(a) shows the $g(r)$ of interstitial impurities ($\lambda' = 2$) for $Q_{gb} = 0.24 \pm 0.02$, and the same quantity is shown in Fig. 7(b) for substitutional impurities ($\lambda' = 3$) at $Q_{gb} = 0.30 \pm 0.03$. Note that, in all of the following, the distance r is expressed in units of σ_s , which corresponds to the lattice spacing at close packing.

Importantly, a first examination of the relative magnitude of the peaks in the $g(r)$ for both

size ratios in Fig. 7(a) and (b) shows that the distribution of impurities is structurally very different from a dilute 2D fluid of hard spheres at the same area fraction.³¹ For instance, in the case of interstitial impurities ($\lambda' = 2$, Fig. 7(a)), the first and second peak have about the same magnitude. Moreover, for substitutional impurities ($\lambda' = 3$, Fig. 7(b)), the first peak is about three times higher than the second. This very likely originates from the depletion forces caused by the host particles,^{29,30,39} leading to

clustering of impurities in the GBs, as expected for systems with negative non-additivity parameters.^{27,28} Note that clustering is facilitated by the fact that the impurities are mobile and thus free to rearrange in the grain boundaries.

We now identify the origin of the peaks in the $g(r)$ for the two size ratios. For the interstitial ($\lambda' = 2$) and substitutional ($\lambda' = 3$) impurities, the first peak of $g(r)$ (I) is located at $r_I \simeq 2.3$ and 4, respectively, which exactly matches the value of $\lambda = 2.26$ and 4, in both cases. This peak thus originates from the direct contact between impurities, as λ is the centre-to-centre distance in this case, and corresponds to *clustering* of the impurities. However, for both size ratios, the second and third peaks (II and III) are not located at integer multiples of λ . They are thus incompatible with direct contact between the impurities and correspond to *mixing* with the host particles.

The relative importance of clustering and mixing seems to strongly depend on the size ratio as suggested by the clear differences in the $g(r)$ for both types of impurities. Indeed, the comparable magnitudes of the first and the second peak in the case of interstitial impurities ($\lambda' = 2$, Fig. 7(a)) suggests the presence of both clustering and mixing. Conversely, the high magnitude of the first peak compared to that of the second for substitutional impurities ($\lambda' = 3$, Fig. 7(b)) indicates a prevalence of clustering. This underlines the importance of geometry in determining the distribution of impurities in our hard sphere system.

Cluster formation

To gain more insight into the role of depletion and clustering in the system, we analyse the clusters formed by both types of impurities. Two impurities are considered to be in the same cluster if their centre-to-centre distance is less than $(r_I + r_{II})/2$. The size distributions of the clusters, $P(s)$, as a function of the size, $s \geq 2$, are presented in Fig. 7(c) and (d) for the two types of impurities, respectively. The insets show the output of the cluster analysis for the images in Fig. 5 at $Q_b = 10^{-1}$. In the case of interstitial impurities ($\lambda' = 2$), the for-

mation of dimers ($s = 2$) is clearly preferred over the formation of clusters of size $s \geq 3$, as inferred from the sharp drop in the probability $P(s)$ above $s = 2$ (Fig. 7(c)). In contrast, the decay of $P(s)$ is much smoother for substitutional impurities ($\lambda' = 3$), which indicates that larger clusters are more frequent in this case (Fig. 7(d)). In the following, we give simple geometric arguments to rationalise the prevalence of dimers in the case of interstitial impurities ($\lambda' = 2$) relative to that of substitutional impurities ($\lambda' = 3$).

Interstitial impurities ($\lambda' = 2$) The first peak of $g(r)$ (I) corresponds to configuration I in Fig. 8(a): the two impurities form a dimer with two host particles on either side. One can see that such a configuration consists of four close-packed particles and for this reason, it is reasonable to expect that their positions can be mapped onto a perfect hexagonal closed-packed lattice. Indeed, it turns out that an equivalent configuration exists on a perfect lattice, with two impurities at interstitial sites and the two side particles in coincidence with crystal sites (see Fig. 8(b)). Note that the location of the two impurities are consistent with their interstitial nature. Using simple geometry, the distance in between the two impurities is found to be $d_I = 4/\sqrt{3} \simeq 2.31$, which is in very good agreement with the experimental location of the first peak, $r_I \simeq 2.3$.

The second peak in $g(r)$ (II) actually consists of a shoulder at $r_{II}^- = 2.9$ and a maximum at $r_{II}^+ = 3$, which correspond to two configurations with no direct contact between impurities. The first configuration, denoted II^- in Fig. 8(a), has a dimer of host particles in between the two impurities. Again, mapping this configuration onto a perfect lattice with the dimer in coincidence with two lattice sites and the two impurities located at interstitial sites leads to an ideal distance of $d_{II}^- = 10/\sqrt{12} \simeq 2.9$, which is in perfect agreement with the observed r_{II}^- . The second configuration, II^+ , corresponds to two impurities sitting at interstitial sites situated on the same row of lattice sites with a triplet of host particles on one side, separated by a distance $d_{II}^+ = 3$ (see Fig. 8(a) and (b)).

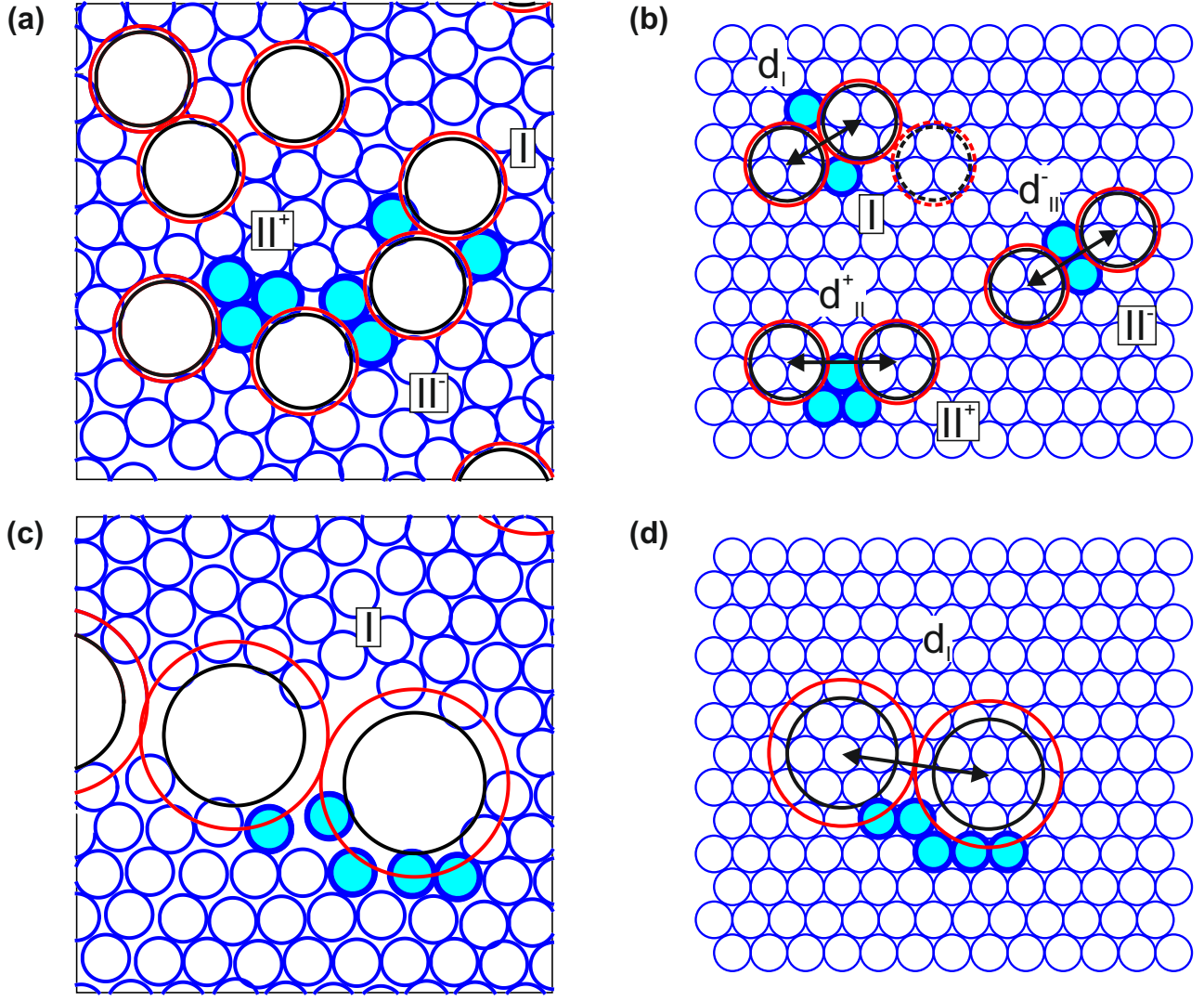


Figure 8: (a) Computer reconstruction of a local view of interstitial impurities ($\lambda' = 2$) segregated at a GB. The three types of configurations contributing to the values of $g(r)$, I, II⁻ and II⁺ are illustrated. (b) The same three configurations but now on a perfect lattice. The particles in coincidence with the lattice are highlighted in cyan and thick circles. This enables geometrically calculating the values of the distances in between impurities, d_I , d_{II}^- and d_{II}^+ . The dashed circles represent one of the few possible ways of adding an impurity to configuration I, due to geometrical restrictions imposed by the lattice. (c) and (d) Same representation for a possible configuration in the case of substitutional impurities ($\lambda' = 3$).

Again, this agrees very well with the observed value for r_{II}^+ .

Importantly, these three configurations (I, II⁻ and II⁺) compete against each other, as their associated values of $g(r)$ are comparable. Configuration I contributes to *clustering*, as it corresponds to direct contact between impurities. However, the lattice geometry strongly restricts the number of possibilities to add more impurities to the cluster (see Fig. 8(b)). This repre-

sents the first source of inhibition for the formation of clusters larger than $s = 2$. The second source is the fact that II⁻ and II⁺ break direct contact between the interstitial impurities, contributing to *mixing* and thus preventing further clustering. These two sources have a clear geometric origin and explain why dimers are relatively more frequent. Both sources of inhibition for the formation of clusters larger than $s = 2$ can be seen as a form of geometric frus-

tration due to the interplay between depletion, non-additivity and lattice geometry.

Substitutional impurities ($\lambda' = 3$) The very high first peak in the $g(r)$ at $r_I \simeq 4$ corresponds to direct contact as it is equal to λ . As the impurities are substitutional, the expected configuration is two impurities located at two crystal sites on the same crystal row separated by a distance $r = 4$. Remarkably, many other configurations like the one presented in Fig. 8(c) are also found. In this case, the mapping onto a perfect lattice in Fig. 8(d) shows that one impurity sits on a crystal site and the other impurity sits at an *interstitial* site, right below the crystal row. The distance between the two impurities is then $d_I = \sqrt{49/3} \simeq 4.04$, which is consistent with a contribution to the first peak, involved in *clustering*. Crucially, these configurations enable impurities to form larger clusters, in contrast with the interstitial impurities. It is also interesting to note that impurities can change from being substitutional to interstitial due to interactions with others impurities.

Conclusion

To summarise, colloidal alloys provide very interesting model systems to study grain boundary segregation using simple video-microscopy. We found that the size ratio between the impurities and the host particles determines the interstitial or substitutional nature of the impurities. In both cases, the adsorption isotherms agree very well with the Langmuir-McLean model of equilibrium grain boundary segregation and the measured free energy of adsorption is small enough to allow for reversible adsorption. We have obtained detailed insight into the configuration of impurities close to saturation of the GBs. The relative balance between clustering and mixing due to non-additivity is found to strongly depend on the type of impurity. This is due to geometrical constraints imposed by the lattice, which prevent the formation of clusters larger than two impurities for interstitial impurities, while for substitutional impurities, the lattice geometry allows

the formation of larger clusters.

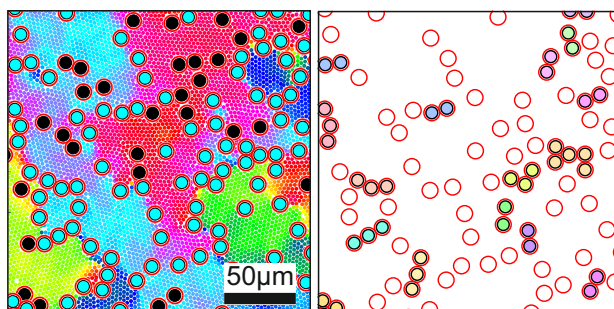
Acknowledgement The authors thank Alice Thorneywork and Roland Roth for useful discussions. The European Research Council (ERC) is acknowledged for financial support (ERC Starting Grant 279541-IMCOLMAT).

References

- (1) Rollett, A.; Humphreys, F. J.; Rohrer, G. S.; Hatherly, M. *Recrystallization and related annealing phenomena*; Elsevier, 2004.
- (2) Cahn, J. W. The impurity-drag effect in grain boundary motion. *Acta Metall. Mater.* **1962**, *10*, 789 – 798.
- (3) Gottstein, G.; Shvindlerman, L. S. *Grain boundary migration in metals: thermodynamics, kinetics, applications*; CRC press, 1999.
- (4) Smith, C. S. Grains, phases, and interphases: an interpretation of microstructure. *Trans. Metall. Soc. AIME* **1948**, *175*, 15–51.
- (5) Nes, E.; Ryum, N.; Hunderi, O. On the Zener drag. *Acta Metall. Mater.* **1985**, *33*, 11 – 22.
- (6) Srolovitz, D. J.; Grest, G. S. Impurity effects on domain-growth kinetics. II. Potts model. *Phys. Rev. B* **1985**, *32*, 3021–3025.
- (7) Hassold, G. N.; Holm, E. A.; Srolovitz, D. J. Effects of particle size on inhibited grain growth. *Scripta Metall. Mater.* **1990**, *24*, 101 – 106.
- (8) Yip, S. Nanocrystals: the strongest size. *Nature* **1998**, *391*, 532–533.
- (9) Schiøtz, J.; Di Tolla, F. D.; Jacobsen, K. W. Softening of nanocrystalline metals at very small grain sizes. *Nature* **1998**, *391*, 561–563.

- (10) Lu, L.; Chen, X.; Huang, X.; Lu, K. Revealing the maximum strength in nanotwinned copper. *Science* **2009**, *323*, 607–610.
- (11) McLean, D. *Grain boundaries in metals*; Monographs on the physics and chemistry of materials; Clarendon Press, 1957.
- (12) Sutton, A. P.; Balluffi, R. W. *Interfaces in crystalline materials*; Clarendon Press, 1995.
- (13) Hondros, E. D.; Seah, M. P. The theory of grain boundary segregation in terms of surface adsorption analogues. *Metall. Trans. A* **1977**, *8*, 1363–1371.
- (14) Seah, M. P. Grain boundary segregation. *J. Phys. F: Met. Phys.* **1980**, *10*, 1043.
- (15) Langmuir, I. The adsorption of gases on plane surfaces of glass, mica and platinum. *J. Am. Chem. Soc.* **1918**, *40*, 1361–1403.
- (16) Barnes, G.; Gentle, I. *Interfacial science: an introduction*; Oxford University Press, 2011.
- (17) Erhart, H.; Grabke, H. J. Equilibrium segregation of phosphorus at grain boundaries of Fe–P, Fe–C–P, Fe–Cr–P, and Fe–Cr–C–P alloys. *Met. Sci.* **1981**, *15*, 401–408.
- (18) Grabke, H. J. Surface and grain boundary segregation on and in iron and steels. *ISI International* **1989**, *29*, 529–538.
- (19) de Villeneuve, V. W. A.; Derendorp, L.; Verboekend, D.; Vermolen, E. C. M.; Kegel, W. K.; Lekkerkerker, H. N. W.; Dullens, R. P. A. Grain boundary pinning in doped hard sphere crystals. *Soft Matter* **2009**, *5*, 2448–2452.
- (20) Yoshizawa, K.; Okuzono, T.; Koga, T.; Taniji, T.; Yamanaka, J. Exclusion of impurity particles during grain growth in charged colloidal crystals. *Langmuir* **2011**, *27*, 13420–13427.
- (21) Ghofraniha, N.; Tamborini, E.; Oberdisse, J.; Cipelletti, L.; Ramos, L. Grain refinement and partitioning of impurities in the grain boundaries of a colloidal polycrystal. *Soft Matter* **2012**, *8*, 6214–6219.
- (22) Yoshizawa, K.; Toyotama, A.; Okuzono, T.; Yamanaka, J. Exclusion of impurity particles in charged colloidal crystals. *Soft Matter* **2014**, *10*, 3357–3361.
- (23) Palberg, T.; Mönch, W.; Schwarz, J.; Leiderer, P. Grain size control in polycrystalline colloidal solids. *J. Chem. Phys.* **1995**, *102*.
- (24) Nozawa, J.; Uda, S.; Naradate, Y.; Koizumi, H.; Fujiwara, K.; Toyotama, A.; Yamanaka, J. Impurity partitioning during colloidal crystallization. *J. Phys. Chem. B* **2013**, *117*, 5289–5295.
- (25) Hu, S.; Nozawa, J.; Koizumi, H.; Fujiwara, K.; Uda, S. Grain boundary segregation of impurities during polycrystalline colloidal crystallization. *Cryst. Growth Des.* **2015**, *15*, 5685–5692.
- (26) Nozawa, J.; Uda, S.; Hu, S.; Fujiwara, K.; Koizumi, H. Orientation-dependent impurity partitioning of colloidal crystals. *J. Cryst. Growth* **2016**, *439*, 13 – 18.
- (27) Hoffmann, N.; Ebert, F.; Likos, C. N.; Löwen, H.; Maret, G. Partial clustering in binary two-dimensional colloidal suspensions. *Phys. Rev. Lett.* **2006**, *97*, 078301.
- (28) Ebert, F.; Maret, G.; Keim, P. Partial clustering prevents global crystallization in a binary 2D colloidal glass former. *Eur. Phys. J. E* **2009**, *29*, 311–318.
- (29) Roth, R.; Evans, R. The depletion potential in non-additive hard-sphere mixtures. *Europhys. Lett.* **2001**, *53*, 271.
- (30) Roth, R.; Evans, R.; Louis, A. A. Theory of asymmetric nonadditive binary hard-sphere mixtures. *Phys. Rev. E* **2001**, *64*, 051202.

- (31) Thorneywork, A. L.; Roth, R.; Aarts, D. G. A. L.; Dullens, R. P. A. Radial distribution functions in a two-dimensional binary colloidal hard sphere system. *J. Chem. Phys.* **2014**, *140*, 161106.
- (32) Blair, D.; Dufresne, E. The Matlab Particle Tracking Code Repository. Retrieved from <http://physics.georgetown.edu/-matlab/>.
- (33) Nelson, D. R. *Defects and geometry in condensed matter physics*; Cambridge University Press, 2002.
- (34) Dillmann, P.; Maret, G.; Keim, P. Polycrystalline solidification in a quenched 2D colloidal system. *J. Phys. Condens. Matter* **2008**, *20*, 404216.
- (35) de Villeneuve, V. W. A.; Dullens, R. P. A.; Aarts, D. G. A. L.; Groeneveld, E.; Scherff, J. H.; Kegel, W. K.; Lekkerkerker, H. N. W. Colloidal hard-sphere crystal growth frustrated by large spherical impurities. *Science* **2005**, *309*, 1231–1233.
- (36) Baumgartl, J.; Dullens, R. P. A.; Dijkstra, M.; Roth, R.; Bechinger, C. Experimental observation of structural crossover in binary mixtures of colloidal hard spheres. *Phys. Rev. Lett.* **2007**, *98*, 198303.
- (37) Gray, A. T.; Mould, E.; Royall, C. P.; Williams, I. Structural characterisation of polycrystalline colloidal monolayers in the presence of aspherical impurities. *J. Phys. Condens. Matter* **2015**, *27*, 194108.
- (38) Higler, R.; Appel, J.; Sprakel, J. Substitutional impurity-induced vitrification in microgel crystals. *Soft Matter* **2013**, *9*, 5372–5379.
- (39) Perera-Burgos, J. A.; Méndez-Alcaraz, J. M.; Pérez-Ángel, G.; Castañeda Priego, R. Assessment of the micro-structure and depletion potentials in two-dimensional binary mixtures of additive hard-disks. *J. Chem. Phys.* **2016**, *145*.



For Table of Contents Only.